Journal of Structural Geology 35 (2012) 90–101

Contents lists available at SciVerse ScienceDirect

Journal of Structural Geology

journal homepage: www.elsevier.com/locate/jsg

Bias due to side wall friction in sand box experiments

P. Souloumiac [a], B. Maillot [a,*], Y.M. Leroy [b]

[a] Département Géosciences et Environnement, Université de Cergy-Pontoise, 5, mail Gay-Lussac, Neuville-sur-Oise, 95031 Cergy-Pontoise, France
[b] Laboratoire de Géologie, CNRS, École Normale Supérieure, Paris, France

ARTICLE INFO

Article history:
Received 24 February 2011
Received in revised form
21 October 2011
Accepted 2 November 2011
Available online 18 November 2011

Keywords:
Analogue modelling
Experimental bias
Sand-box experiments
Sand-glass friction

ABSTRACT

The principal concern of this paper is with the accuracy and validity of experimental sand box models of geological structures – and of thrust faults in particular – as influenced by side wall friction. Side wall friction can produce undesirable artifacts, in particular in experiments aimed at reproducing plane deformations. The importance of such artifacts is revealed in the present study by the results of experiments that are affected in opposite ways by side wall friction. Two distinct experimental configurations have been chosen for this purpose for a set-up that comprises a body of sand placed between vertical side walls on a basal plate against a back wall and a front wall, all made of glass. In configuration M the bottom plate and attached front wall move relative to the side walls towards a fixed back wall, while in configuration F the back wall moves relative to the side walls and attached bottom plate towards a fixed front wall ('fixed' = 'fixed relative to the side walls'). In both configurations, thrust traces on the top surface of the sand become curved near the side walls because of wall friction. The outcome of altogether 31 experiments in the two configurations shows that the magnitude of the experimental bias depends on the ratio S_L/S_B of the area of contact of the sand body with the side walls (S_L) to its area of contact with the basal surface (S_B). The bias is the difference in thrust locations in the two configurations. It is measured on photographs taken through the side walls during the experiments. Away from the side walls, the bias is estimated by the thrust curvatures observed in top views. For $S_L/S_B \leq 0.1$, i.e. very little contact with side walls, there is no identifiable bias. Furthermore, a 2D theoretical solution reproduces well the results. For S_L/S_B increasing to 0.25, curvatures increase, yielding rather different cross-sections at the side walls, but still similar cross-sections in the central part of the sand body. For $S_L/S_B \geq 0.3$, thrust planes occupy different regions of the box for each configuration, although their curvature is decreasing. At $S_L/S_B = 0.9$, curvatures have almost disappeared but the location of the thrusts and the length of the décollement depend strongly on the experimental configuration. Departures from the 2D theoretical solution are clearly stronger with configuration M than F. Another important conclusion is that the absence of curvature of the thrust traces is not a proof of the 2D character of the experiment. Mechanical equilibrium of the total forces recorded at both front and back walls during shortening shows that the thrust locations are controlled by the difference between basal and side wall shear forces.

1. Introduction

Geological structures are often affected by 3D effects that can control spacing, position and also style of faults. Various factors can be at the origin of these 3D effects such as the thickness of sediments (Marshak and Wilkerson, 1992), the influence of erosion and transport on topography (Marques and Cobbold, 2006), or the geometry of ramps (Wibberley, 1997). Thus, an analogue experiment supposed to reproduce natural observations shall remain a 3D physical problem. And yet most of analogue studies intend to reproduce 2D cross sections rather than real 3D geological structures because it is a very useful simplification to consider that the main features of a structure are 2D, and that 3D effects are only added perturbations. In any case, one should make sure that the experimental results do not suffer from spurious 3D effects due to the experimental set-up rather than to natural causes. Since most experimental set-ups use side walls, which apply efforts on the analogue material, their influence on structural deformations cannot be neglected. It seems essential to quantify these 3D lateral effects, firstly to improve the fit between experiments and real structures and secondly to understand variability of outcomes between different experimental set-ups.

3D structures considerations, focussing on lateral effects in analogue models, have been discussed before by Costa and

* Corresponding author. Tel.: +33 134257359; fax: +33 134257350.
E-mail address: bertrand.maillot@geol.u-cergy.fr (B. Maillot).

0191-8141/$ – see front matter © 2011 Elsevier Ltd. All rights reserved.
doi:10.1016/j.jsg.2011.11.002

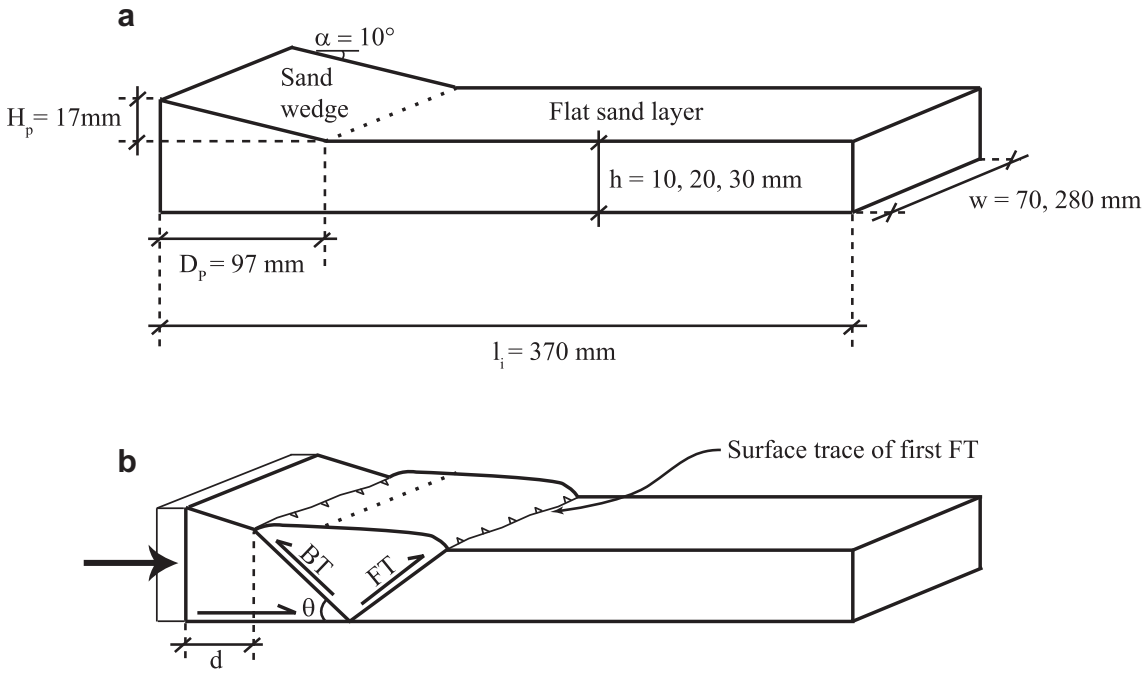

Fig. 1. a) Initial geometry of the sand body used in all experiments. The thickness *h* of the flat sand layer may be 1, 2, or 3 cm. Two boxes are used, to change the width *w* from 7 cm to 28 cm. b) *d* is the position of the first pop-up structure, measured on side view photographs after 11 mm of shortening. "BT" and "FT" denote respectively backthrust and forethrust.

Vendeville (2004) and Koyi and Cotton (2004). In the particular case of very low basal shear forces (using viscous PDMS), the lateral walls can control entirely the evolution of thrust sequences (Vendeville, 2007). The benchmark of Schreurs et al. (2006) highlights large differences in model evolution due to different experimental set-ups. Several laboratories performed the same brittle thrust wedge experiment, with their own apparatus and material. Comparisons of final model states reveal significant variations on the number, position and dips of thrusts that were attributed to six experimental issues. Choosing an experimental set-up that comprises a body of sand placed between vertical side walls on a basal plate against a back wall and a front wall, we shall address the following three of these issues in this paper: boundary conditions at the side walls, width of the sand box, and location of the observed feature (along side walls, at the top surface of the sand). The prototype used is a flat sand layer topped by a triangular sand wedge and subjected to shortening. It is very similar to the prototypes proposed by Dahlen (1984) and Schreurs et al. (2006).

The next section presents the set-up and the prototype. The third section consists of an analysis of the first fault system after an applied shortening of 11 mm, followed by an analysis of the final deformations, and of the evolution of forces at the back and the front walls measured by strain gauges during the applied shortening. In the Fourth section we discuss the experimental result. The forces allow us to understand the frictional effects of the lateral walls by simple equilibrium conditions. We compare the results to a 2D theoretical solution of the onset of thrusting (Appendix) that is a generalisation based on limit analysis, of the critical prism theory to prisms with an accreting flat sand layer.

2. Description of the experiments

The experiments consist in shortening lengthwise a uniform sand body made of a flat layer occupying all the experimental box, and a wedge on one side (Fig. 1a). Two distinct experimental configurations have been chosen for a set-up that comprises the body of sand placed between vertical side walls on a basal plate against a back wall and a front wall, all made of glass. In configuration M (Fig. 2) the bottom plate and attached front wall move relative to the side walls towards a fixed back wall, while in configuration F (Fig. 2b) the back wall moves relative to the side walls and attached bottom plate towards a fixed front wall ('fixed' = 'fixed relative to the side walls').

Measurements of forces at both front and back ends of the sand body during shortening provide rich information. Strain gauges are placed behind the front and back walls to measure the force they sustain during shortening (details in Cubas, 2009; Cubas et al.,

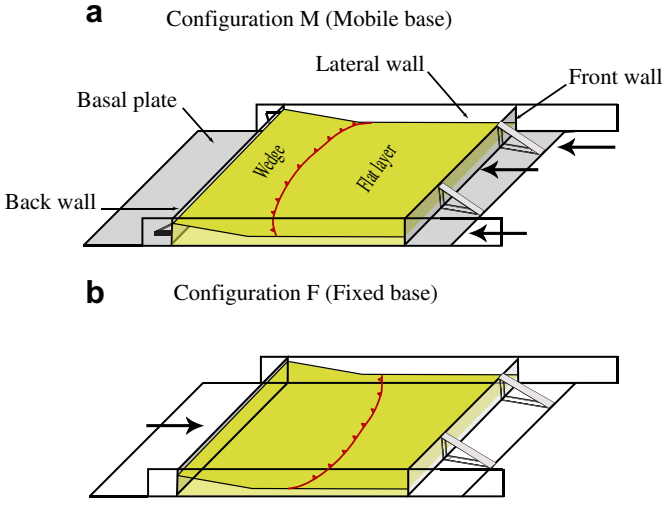

Fig. 2. Schematic oblique view of the experimental box. The front wall and the basal plate are attached together. In configuration M, the front wall and the basal plate (in grey) move together during the applied shortening (arrows, from right to left). In configuration F, the back wall (in grey) is the only mobile part (arrow from left to right). Typical thrust curvatures due to lateral friction are shown in each case by the curved solid lines between the wedge and the flat layer regions.

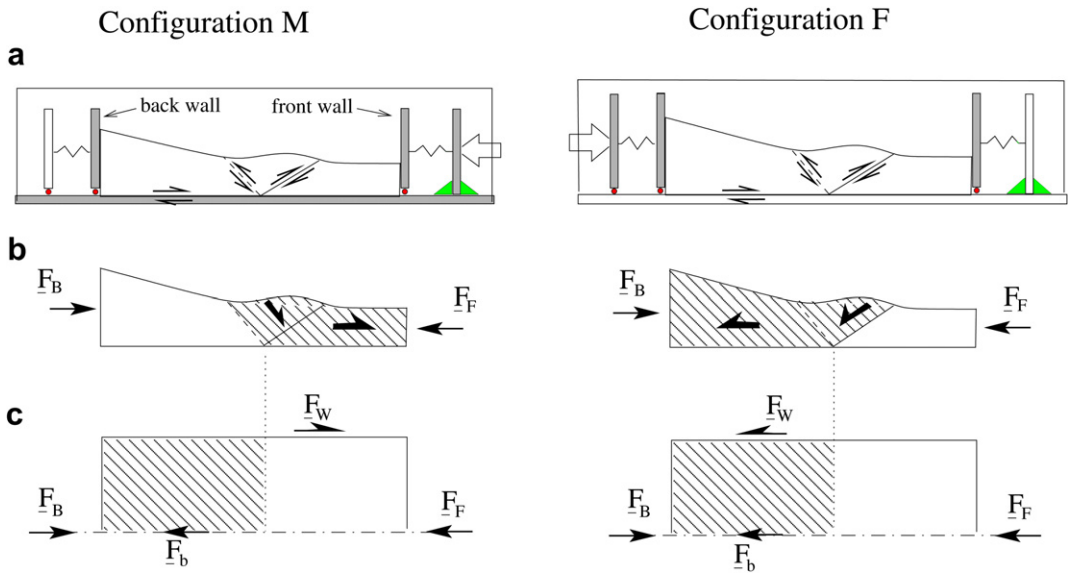

Fig. 3. The measurement of forces is done by strain gauges placed behind the front and the back walls. Moving parts are in grey, ball (red) contacts are lubricated, black triangle (green) contacts are rigid. The empty arrows recall the applied shortening, and the semi-arrows, the sense of shear on each active thrust. In b) (cross-section at a side wall) and c) (top view of basal plate), the hashed regions are the areas where sand slides with respect to the lateral walls and the basal plate, respectively. The semi-arrows illustrate the direction and sense of shear exerted by the side walls on the sand body ($\mathbf{F}_W$). $\mathbf{F}_b$ is the shear exerted by the basal plate, and $\mathbf{F}_B$ and $\mathbf{F}_F$ are respectively the forces sustained by the back and front walls, and measured by the strain gauges. Note that $\mathbf{F}_W$ is acting on different regions of the sand body, and in opposite senses, in configurations M and F. In c), only half of the box is drawn (the dash-dotted line is the line of symmetry). (For interpretation of the references to colour in this figure legend, the reader is referred to the web version of this article.)

2010). For technical reasons, the absolute values of the forces cannot be interpreted with confidence, we therefore present them with the raw units of the strain gauge software.

In order to help interpretation of the force measurements, that will be presented in Section 4, we present some theoretical relationships between the forces measured at the two end walls. For the body to be in global equilibrium, the weight **W** of the sand, the forces $\mathbf{F}_F$ and $\mathbf{F}_B$ transmitted by the front and back walls, and the forces $\mathbf{F}_W$ and $\mathbf{F}_b$ transmitted by the side walls and by the bottom plate must sum up to zero, giving

$$\mathbf{W} + \mathbf{F}_B + \mathbf{F}_F + \mathbf{F}_b + \mathbf{F}_W = 0. \quad (1)$$

Projecting forces in the direction of shortening (assumed horizontal), chosen positive from the wedge side to the flat layer side (i.e., to the right in Fig. 3), yields the equilibrium conditions

$$F_B - F_F = F_b - F_W, \quad \text{for configuration M, and} \quad (2)$$

$$F_B - F_F = F_b + F_W, \quad \text{for configuration F,} \quad (3)$$

where F_B, F_F, F_b, F_W are positive scalars of magnitude equal to the horizontal projections of the corresponding force vectors in equation (1). These highlight the opposite effect of lateral friction in each configuration: in configuration M, the shear on the lateral walls F_W acts globally in the same sense as the shortening force F_B; while in configuration F, the lateral shear is opposite to the shortening. Ideally, if the lateral walls were perfectly lubricated, $\mathbf{F}_W$ would be perpendicular to the lateral walls, and would disappear from the equilibrium conditions (2) and (3) which would be the same for both configurations. We further define the mean dimensionless horizontal force during shortening as

$$\overline{F}_H = \frac{1}{\delta_T}\int_0^{\delta_T} (F_B - F_F)\mathrm{d}\delta, \quad (4)$$

because it will help the interpretation of the force measurements.

We used a single batch of Fontainebleau aeolian quartz sand (99.7% of quartz). The median grain size is 250 μm with 95.5% in mass of grain sizes comprised between 150 and 425 μm. This sand was found previously to have a peak friction of 33° weakening to 30° over a slip of 3 mm for a newly formed slip surface, and 1 mm

Table 1
Experimental set-ups and outcomes.

Exp. nbr.	w (cm)	h (cm)	δ_T (cm)	Wall config.	S_L/S_B	$\bar{d}$	θ (deg)	$\overline{F}_H$
77	28	1	3	M	0.09	0.86	36.5	565
80	28	1	3	M	0.09	1.03	39	604
89	28	1	3	M	0.09	1.08	32.2	794
82	28	1	3	F	0.09	0.96	44	468
86	28	1	3	F	0.09	0.84	38	468
75	28	2	5	M	0.16	0.94	32.4	–
76	28	2	5	M	0.16	1.16	31.8	1197
88	28	2	5	M	0.16	1.16	32.1	1189
79	28	2	5	F	0.16	0.91	39	1070
83	28	2	5	F	0.16	0.90	35	1126
71	28	3	6	M	0.23	1.17	32	–
72	28	3	6	M	0.23	1.41	32.4	1155
74	28	3	6	M	0.23	1.37	31.3	1488
81	28	3	6	M	0.23	1.36	34.3	1366
85	28	3	6	F	0.23	1.00	33	1798
87	28	3	6	F	0.23	0.92	33.5	1771
172	28	3	6	F	0.23	0.78	–	–
98	7	1	3	M	0.35	1.46	36	97
169	7	1	3	M	0.35	1.10	38	–
97	7	1	3	F	0.35	0.97	37	330
171	7	1	3	F	0.35	1.03	41	–
78	7	2	5	M	0.64	1.32	34.8	–
93	7	2	5	M	0.64	1.48	34.5	9.7
99	7	2	5	M	0.64	2.76	33.7	32
101	7	2	5	M	0.64	1.35	33.7	64
94	7	2	5	F	0.64	0.58	31.5	505
100	7	2	5	F	0.64	0.75	36.7	384
95	7	3	6	M	0.92	2.56	34.3	−66
168	7	3	6	M	0.92	2.61	31.5	–
96	7	3	6	F	0.92	0.34	37	804
170	7	3	6	F	0.92	0.11	32.5	–

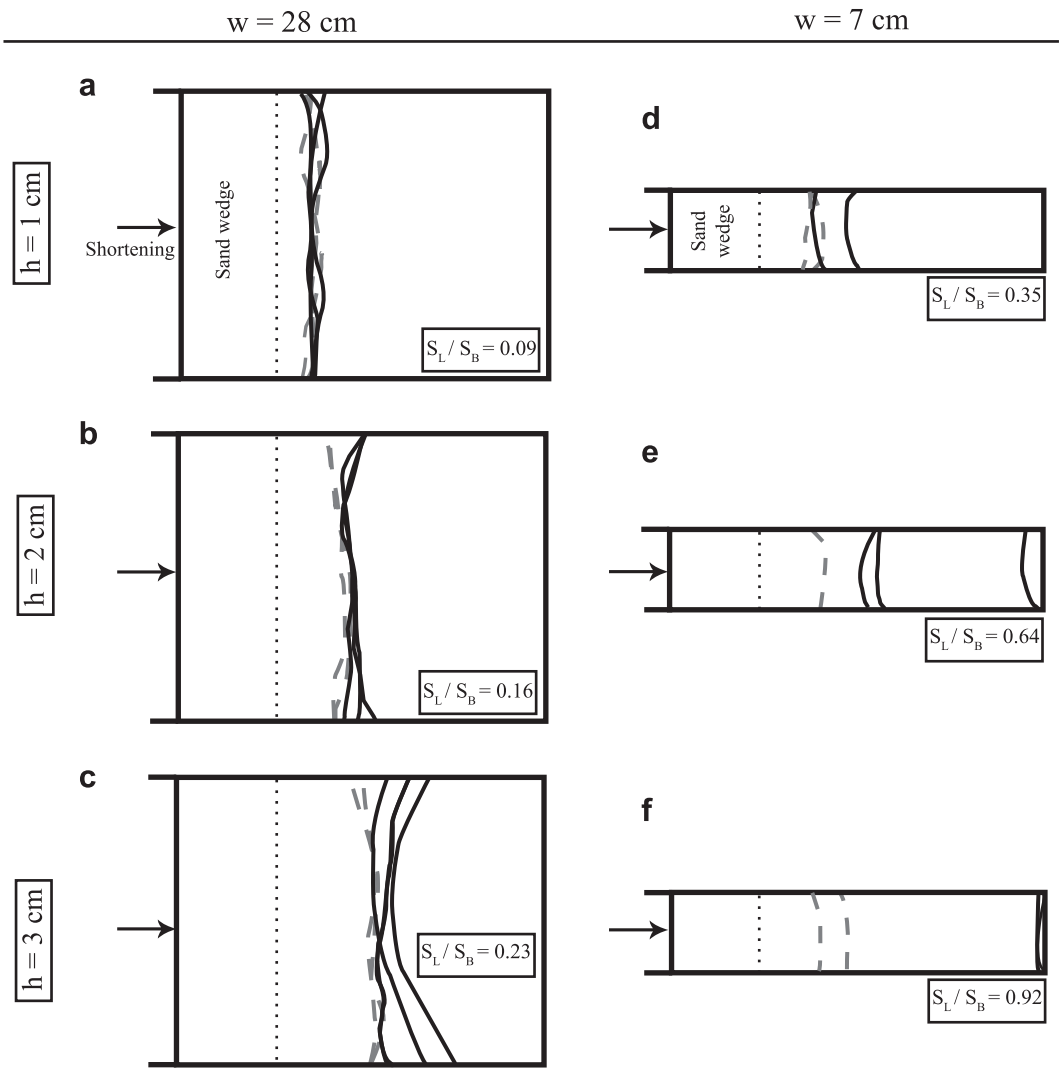

Fig. 4. Top view drawings of the emergence of the first forethrust in all experiments after 11 mm of shortening (Fig. 1b) (top view data lacked in three experiments). Solid lines: configuration M, dashed lines: configuration F. Same curve types in each drawing represent repeated experiments using the same set-up. Tip of the initial sand wedge is indicated by the dotted line. a) to c): wide box ($w = 28$ cm) with increasing thickness of the flat sand layer from 1 to 3 cm. d) to f): same as a) to c), using the narrow box ($w = 7$ cm). Note the increasing value of the ratio S_L/S_B from a) to f).

for reactivation of an existing slip surface (Klinkmüller et al., 2008). All walls are treated with a carbon based product ("RainX", manufactured by Shell Research Intl.) and yield a friction angle of 7.5° to 10° (coefficients of 0.13–0.18) and a negligible cohesion of about 10 Pa. The sand pack was built with a dedicated sand distributor adapted from Wygal (1963). Sand packing is dense, reproducible, and homogeneous throughout the box with a material density of 1710 ± 6 kg/m^3 (Cubas et al., 2010). The temperature in the laboratory varied between 17.5° and 22.5°, and the relative humidity, between 60% and 80%.

A series of 31 experiments were conducted, using twelve different set-ups (Table 1) which vary by the width w of the box, the thickness h of the flat layer, the total applied shortening δ_T, and the configuration of the lateral walls (M or F). S_L/S_B is the ratio of lateral (S_L) to basal (S_B) areas of sand in contact with the two lateral walls and the basal plate, respectively. It is calculated from l_i, w, h, D_p and H_P (Fig. 1a). The last three columns of Table 1 are experimental outcomes and will be dealt with in the next sections. Two to four experiments were performed with each set-up to demonstrate the reproducibility of the results.

3. Thrusting sequences

3.1. Onset of thrusting

After 11 mm of applied shortening, the initial diffuse horizontal compaction of the sand has been localised into a well formed forethrust–backthrust pair in all experiments. The sand wedged between them forms a pop-up structure. These two thrusts merge at the basal plate at a position corresponding to the end of the active décollement (semi-arrows in Fig. 1b).

3.1.1. Top views

The surface trace of the first forethrust (Fig. 1b) is drawn after top view photographs (Fig. 4). In the wide box, at the lowest value of S_L/S_B ($S_L/S_B = 0.09$, Fig. 4a), surface traces using configurations M and F are almost undistinguishable. An increasing divergence of the curvature of the traces between the results of configuration M and F is clear, especially towards the lateral walls, for $S_L/S_B = 0.16$ and 0.23 (Fig. 4b, c). In the narrow box (Fig. 4d–f), the traces for the two configurations differ increasingly with increasing ratios S_L/S_B, such

that the forethrusts appear at completely different positions when $S_L/S_B = 0.92$. This difference is mainly due to change of the forethrust position in configuration M towards the front wall. In configuration F, forethrusts have more stable locations from a) to f), and thus appear less sensitive to the S_L/S_B ratio. Note also that in the narrow box, thrust traces are more regular, exhibiting a nearly 2D plane-strain geometry.

3.1.2. Side views

Side views through the lateral walls in configuration M are shown in Fig. 5 (ordered by increasing values of the S_L/S_B ratio, as in Fig. 4), and those in configuration F, in Fig. 6. From a) to f), the pop-up structure forms more and more ahead of the initial wedge tip in configuration M (Fig. 5). In configuration F, the pop-up is more stable, but tends to appear closer and closer to the back wall (Fig. 6).

From both top and lateral views, we conclude that the first pop-up structure is displaced in opposite directions in configuration M and F towards the front wall and back wall respectively, depending on the thickness h and width w. The displacement in configuration M is larger than in configuration F. These observations are quantified in Fig. 7 using the horizontal distance from the back wall to the emergence of the backthrust at the sand surface (d in Fig. 1b), measured on the photographs of Figs. 5 and 6. It is striking to note that all (but two) experiments using configuration M produce pop-ups ahead of the wedge tip ($d \geq 10$ cm), while those in configuration F always yield $d \leq 10$ cm. The effect is more pronounced in the narrow box ($w = 7$ cm), calling for another representation of the data, that combines h and w through the ratio S_L/S_B.

In Fig. 8, we show the value of $\tilde{d} = d/D_P$ (Table 1, D_P is the length of the initial sand wedge, Fig. 1a) in each experiment as a function of S_L/S_B. At the lowest value, $S_L/S_B = 0.09$, measurements made in both wall configuration (M: circles, F: crosses) are well grouped close to the value of one. For $S_L/S_B = 0.16$ and 0.23, divergence between configurations M and F becomes clear, mainly because configuration M measurements increase. This tendency continues in the narrow box, for $S_L/S_B = 0.35$. At $S_L/S_B = 0.64$, one experiment exhibits a large translation of the thrust, to the frontal end of the box, as was seen in Fig. 4e. At the value of 0.92, finally, the two

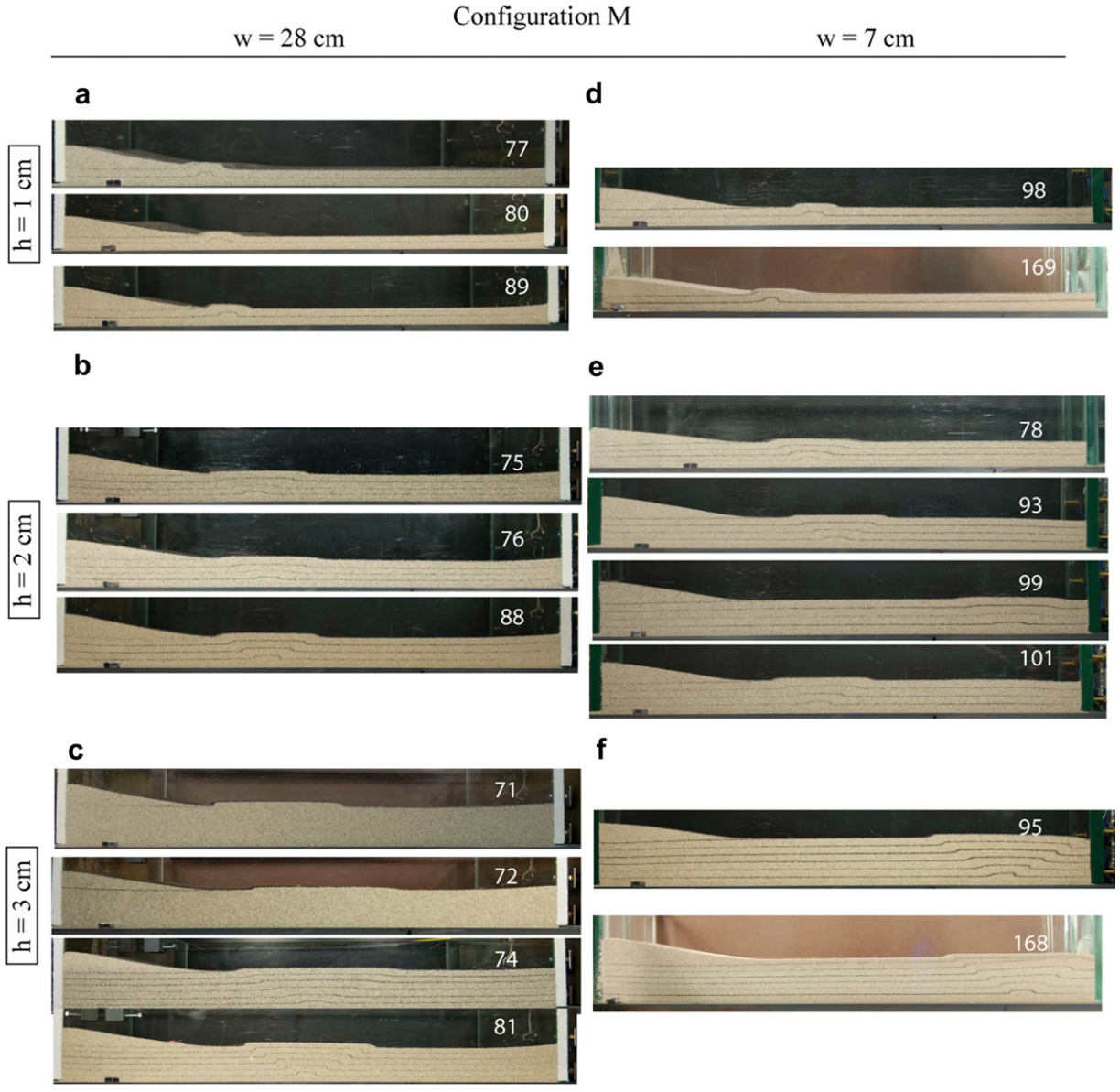

Fig. 5. Views through a lateral glass wall after 11 mm of applied shortening, for all experiments in configuration M. Same values of the ratio S_L/S_B from a) to f) as in Fig. 4.

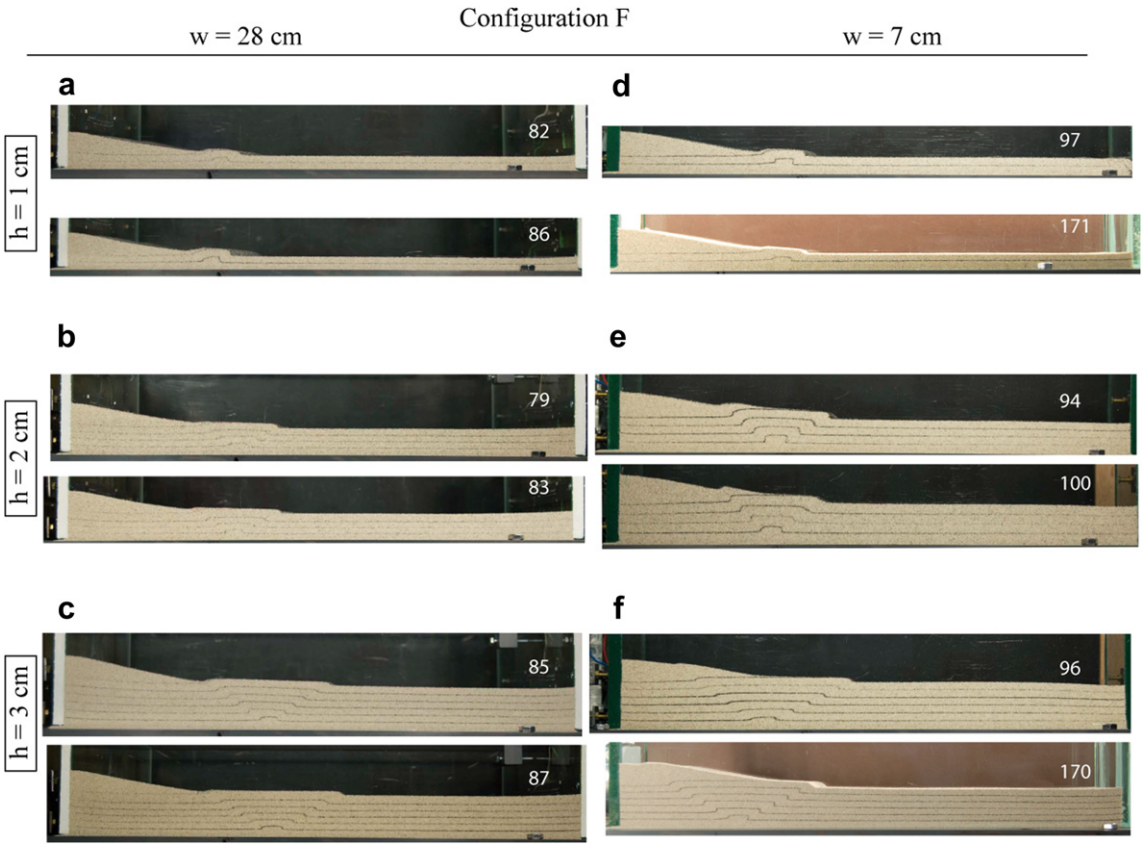

Fig. 6. Views through lateral glass wall after 11 mm of applied shortening for all experiments in configuration F.

configurations yield completely different locations for the initiation of thrusting.

This increasing difference in pop-up location is further illustrated by plotting the absolute value of the difference between the values of $\tilde{d}$ in each configuration, named the experimental bias (Fig. 9). Since several experiments were conducted in each set-up, we plot the maximum, minimum, and mean differences. We note first that the bias tends to zero when S_L/S_B tends to zero, and increases with S_L/S_B. The increase is roughly bilinear, with a slope of 1.1 for $S_L/S_B \leq 0.5$, and 4.4 for $S_L/S_B \geq 0.5$. The slight decrease from $S_L/S_B = 0.23$ to 0.35 corresponds to the change of box from 28 cm width to 7 cm. For $S_L/S_B \geq 0.6$ the bias becomes very large, comparable to the length D_P of the initial wedge. However, since forethrusts reached the frontal end of the box, the value of the bias is limited by the length of the box: it would be even greater in a longer box.

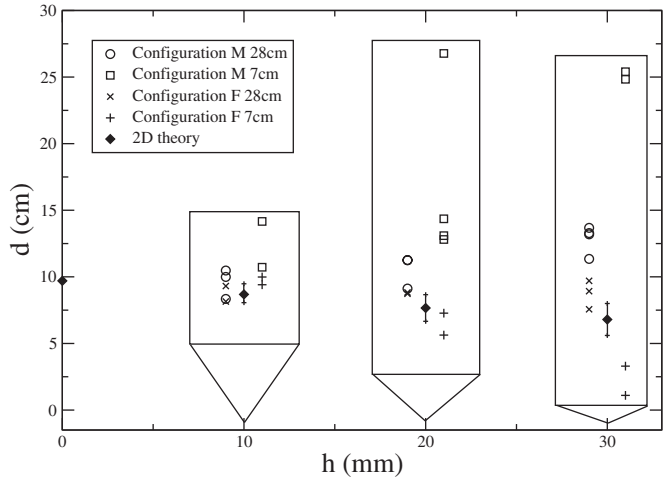

Fig. 7. Position of the first pop-up structure (d in Fig. 1b) in all experiments after 11 mm of shortening, as a function of the initial layer thickness h (Fig. 1a). The 2D theoretical values are from limit analysis, see Appendix. Symbols are spread laterally in the boxes, for clarity.

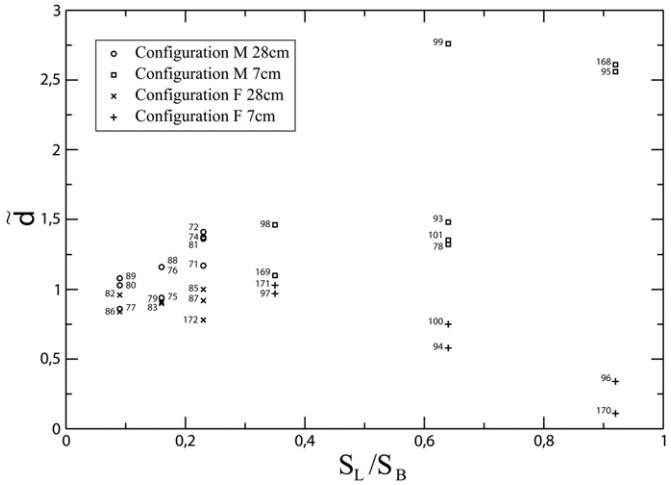

Fig. 8. Dimensionless length of décollement ($\tilde{d} = d/D_P$, Fig. 1) versus ratio between lateral (S_L) and basal (S_B) areas of sand (Table 1). Numbers refer to each experiment of this study (Table 1).

3.2. Thrusting at the end of shortening

The total applied shortening δ_T varies from 3 cm to 6 cm depending on the thickness h (Table 1). Views through a side wall in the final states are shown for all experiments in Figs. 10 (conf. M) and 11 (conf. F). Comparison of Fig. 10a–f with Fig. 11a–f shows that the bias seen previously after 11 mm of shortening is confirmed here, increasing from a) to f). In a), it is not visible, while in f), it completely controls the position of the pop-up (at opposite ends of the box in configurations M and F). In the case $h = 2$, $w = 28$ cm (Fig. 10e), all experiments developed two pop-up structures, but in an opposite sequence for Exp. 99 (circled numbers indicate the order of formation of the pop-ups).

Overall, the M configuration is seen to promote a deformation well ahead of the initial prism as S_L/S_B increases. In contrast, the deformation is favoured in the vicinity of the back wall and of the initial prism in configuration F. The measurements of forces will help explain these observations.

3.3. Forces on front and back walls

We have selected the four set-ups with the greatest S_L/S_B ratios ($h = 2$ and 3 cm; $w = 7$ cm; conf. M and F; Exp. 99, 95, 100 and 96) to present the force measurements. In exp. 96 (Fig. 12), the force at the back wall shows first a rapid increase from 0 to 1100 due to the elastic loading of the strain gauges, then a decrease to 750 corresponding to the formation of the pop-up structure (at 10 mm of shortening), then a slow increase followed by a slow decrease back to 750 to reach a minimum corresponding to the formation of a second backthrust (at 30 mm), and finally a continuous increase until the end of the experiment. Thus, each decrease corresponds to the formation of a thrust, while the slow increase is due to the formation of the relief. All experiments exhibit similar variations correlating with thrust formation, in the forces at the back wall. This is a consequence of the strain weakening in the sand during localisation of deformation into thrusts. This behaviour has long been known in soil mechanics, and was first measured in a sand box by Nieuwland et al. (2000) who used sensors embedded in the sand. Recall that our initial sand pack is quite dense (1710 kg/m^3, i.e. a porosity of 35%) and therefore some dilatancy is necessary to create thrust planes, explaining the observed strain weakening. Readers my gain more insights on these questions by reading Bjerrum et al. (1961), Krantz (1991), Lohrmann et al. (2003), and references therein.

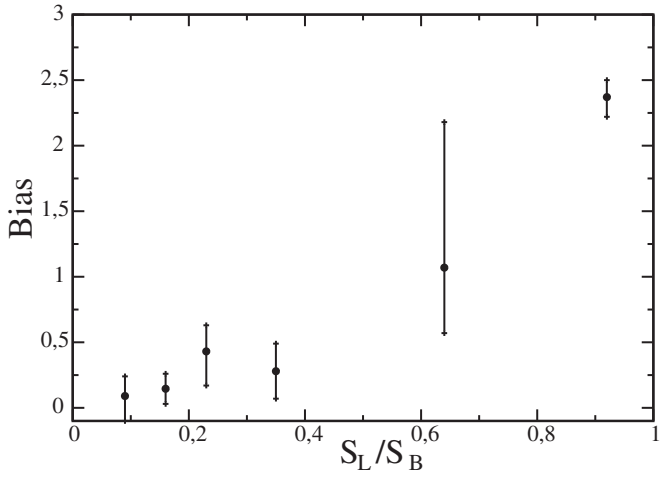

Fig. 9. The bias is the absolute difference between the position of the pop-up ($\bar{d}$) using configuration F and M (Fig. 8). The dot is the mean value of the difference, the two crosses indicate the maximum and minimum values observed when repeating the experiments.

In Exp. 96 and 100 (Figs. 12 and 13), the force at the front wall is negligible compared to that at the back wall. In contrast, in Exp. 95 and 99 (Figs. 14 and 15), conducted in configuration M, the force at the front wall is almost equal to that at the back wall, and displays the same variations with thrusting.

4. Interpretation and discussion of observed thrusting sequences

4.1. Reproducibility

Experimental reproducibility is satisfactory as same curve types (i.e., using same set-up) are very close in all drawings of Fig. 4. The same conclusion can be drawn from the photos of Figs. 5 and 6. The displayed variability using the same set-up is generally smaller than changes between set-ups. The case $w = 7$ cm, $h = 2$ cm, Figs. 4e and 5e, exp. 99, is an exception and seems to represent a sort of bifurcation in the sand pack behaviour, between results for $h = 1$ cm and $h = 3$ cm. This observation will be explained below, in the light of force measurements. At the end of shortening, variability of results is of course greater than at 11 mm of applied shortening, showing sometimes one, sometimes two pop-up structures (compare exp. 77 with exp. 80, or exp. 98 with exp. 169, Fig. 10 a and d). Also, as could have been deduced from the observations at 11 mm of shortening, variability is greater in configuration M (Fig. 10) than in configuration F (Fig. 11) where one finds the same number of pop-ups in each experiment using the same set-up.

4.2. Analysis of force measurements

For $S_L/S_B < 0.4$, friction on the side walls is compensated by thrust curvature. For $S_L/S_B > 0.6$ in configuration M, thrust curvature is insufficient and the thrusts change of position, producing a large bias (Fig. 9). The stress field is perturbed throughout the box. This intuitive statement is supported by the force measurements. In Exp. 96 and 100 (Figs. 12 and 13), the negligible value of the force at the front wall compared to that at the back wall means that the imposed compression at the back wall is fully balanced in the sand body by friction on the base and side walls (equation (3)). In contrast, in Exp. 95 and 99 (Figs. 14 and 15), conducted in configuration M, friction forces on basal and side walls tend to cancel each other in the global force balance of the sand body (2). The body must in turn develop a strongly 3D stress field connecting the side and basal walls, to ensure local stress equilibrium. Indeed, sliding of sand against the side walls occurs between the active forethrust and the front wall, i.e., along most of the lateral areas, whereas in configuration F, sliding occurs mostly close to the back wall, and disappears ahead of the active forethrust (Fig. 3b). Therefore, the compressive stress field extends much further ahead of the prism in configuration M than in F (compare forces at the front wall in Figs. 14 and 15 to Figs. 12 and 13), and promotes thrusting towards the frontal end of the box. It is striking to note that experiments 95 and 99 also exhibit little lateral variation of the thrusts (Fig. 4e and f, solid curves). This 2D plane-strain character coincides in fact with strong friction effects from the side walls, dictating the position of thrusts.

More generally, for all set-ups, the difference between the values of $\overline{F}_H$ in configurations M and F (equations (2)–(4)), is strongly correlated to the position of the pop-ups. The values of $\overline{F}_H$ using configuration F and M are comparable when $S_L/S_B \leq 0.16$ (Table 1), i.e. when the bias is negligible or small. For $S_L/S_B \geq 0.23$, $\overline{F}_H$ using configuration F is always greater than with configuration

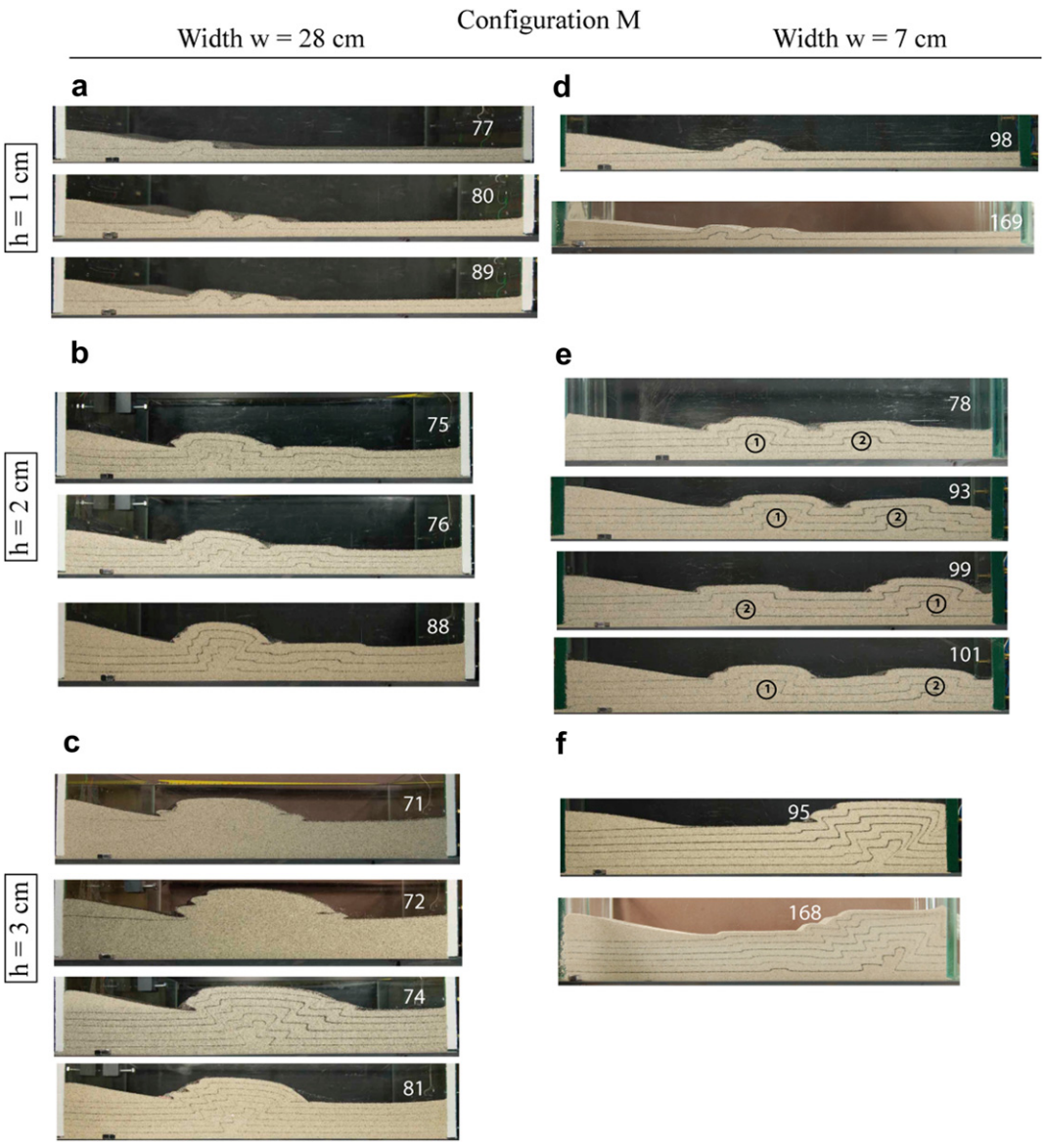

Fig. 10. Views through lateral glass wall at the end of the applied shortening (δ_T in Table 1), for all experiments using configuration M.

M. This observation proves that lateral friction forces F_W become more and more important compared to basal friction forces F_b, as S_L/S_B increases, and offers therefore an explanation for the increasing bias.

The actual value of $\overline{F}_H$ is also informative. Whenever $\overline{F}_H$ has a large positive value, $F_B \geq F_F$, so that stress in the sand body is concentrated towards the back wall. In such experiments, the pop-up structure develops on the back wall side, around the tip of the initial sand wedge (e.g., Figs. 12 and 13). When $\overline{F}_H$ is close to zero (Fig. 15), the pop-up may appear anywhere between the initial wedge and the front wall. This is the case for all experiments of Fig. 10e, which displayed pop-ups at the wedge, and at the front wall, in a normal or reversed sequence, in the final state. Finally, when $\overline{F}_H$ is negative, the pop-up is at the front of the box (Fig. 14). The most spectacular effect is when a spontaneous wedge is growing with an opposite slope to the initial wedge (Fig. 10f). In the 2D critical prism theory this would appear as a critical wedge with a negative taper angle! The structure is therefore completely controlled by the friction on the lateral walls.

4.3. Comparison to a 2D theoretical prediction

The theoretical outcome of such experiments is well known, in the absence of the flat layer: the critical prism theory predicts that the wedge will either deform to increase its taper angle to the critical value, or slide without internal deformation if its taper angle is greater than the critical value. Under the chosen experimental conditions, the wedge, with a surface slope of 10°, should slide without internal deformation, because its taper is much greater than the critical value below which internal deformation occurs. In the case of a sand wedge without flat layer ($h = 0$), the 2D theoretical result, from the critical prism theory, is $d = D_P = 97$ mm ($\tilde{d} = 1$). In the presence of a flat layer, thrusting should occur close to the wedge tip (Fig. 1b), but how close? 2D numerical simulations of similar experimental set-ups display solutions with varying amounts of diffuse deformation prior to thrusting, and thrusting structures containing a forethrust, but not always a backthrust (Buiter et al., 2006, Fig. 2b, c). They do not show enough convergence towards a unique solution to be useful here. The simulation

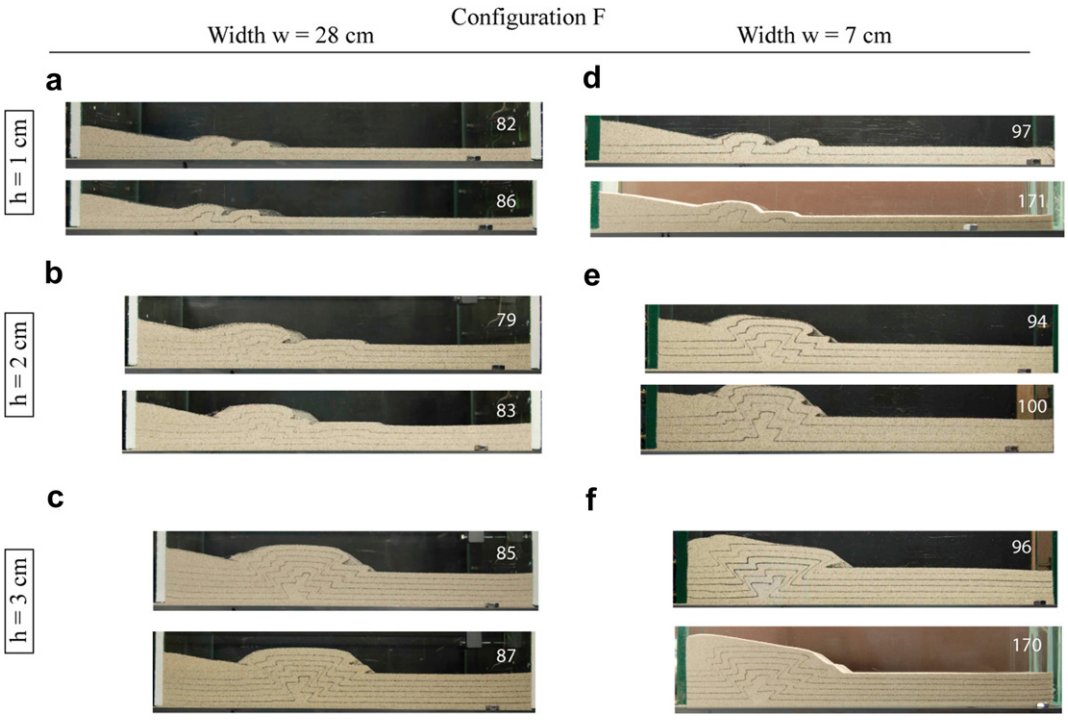

Fig. 11. Views through lateral glass wall at the end of the applied shortening (δ_T in Table 1) for all experiments using configuration F.

by Egholm et al. (2007, Fig. 5a) using a distinct element method does show similarity with our Fig. 6c, f, and less similarity with the configuration M (Fig. 5c, f). Note that they used a higher basal friction (20°). In order to obtain predictions for all set-ups, we shall turn to limit analysis (Cubas et al., 2008) as outlined in the Appendix. It offers a simple way to predict location of the onset of thrusting in a 2D version of our set-ups, and allows us to generalise the stability predictions of the critical wedge theory, to a wedge with an accreting layer. Assuming an internal friction angle for the sand of 30° to 35°, zero cohesion, and a friction angle against the glass of the box of 8° to 10°, the theory predicts a linear decrease of d with h: $d = D_P = 97$ mm ($\tilde{d} = 1$) for $h = 0$ mm; $d = 87 \pm 8$ mm ($\tilde{d} = 0.9 \pm 0.08$) for $h = 10$ mm; $d = 77 \pm 10$ mm ($\tilde{d} = 0.8 \pm 0.1$) for $h = 20$ mm; and $d = 68 \pm 12$ mm ($\tilde{d} = 0.7 \pm 0.12$) for $h = 30$ mm. These values are indicated as black diamonds with error bars in Fig. 7. Clearly, as h increases, the experiments diverge from the 2D theory, and those in configuration M and using the

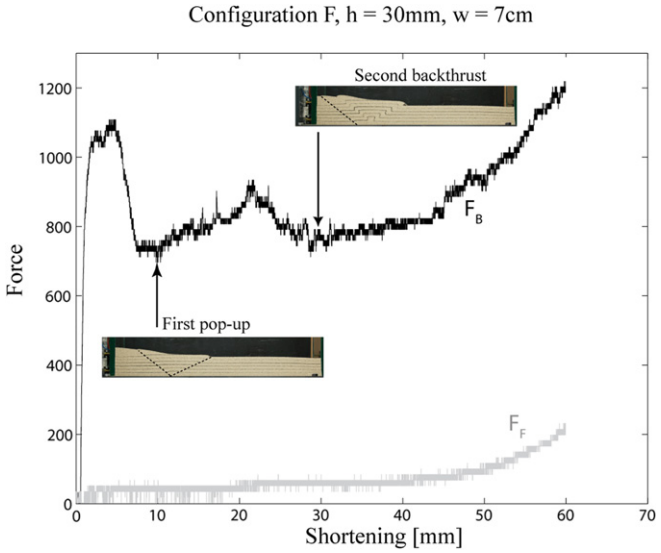

Fig. 12. Dimensionless force versus displacement in experiment 96 and associated views through a lateral wall. F_B is the force at the back wall (left wall in the photos), F_F is the force at the front wall. The mean difference between the two curves is $\bar{F}_H = 804$ (equation (4)).

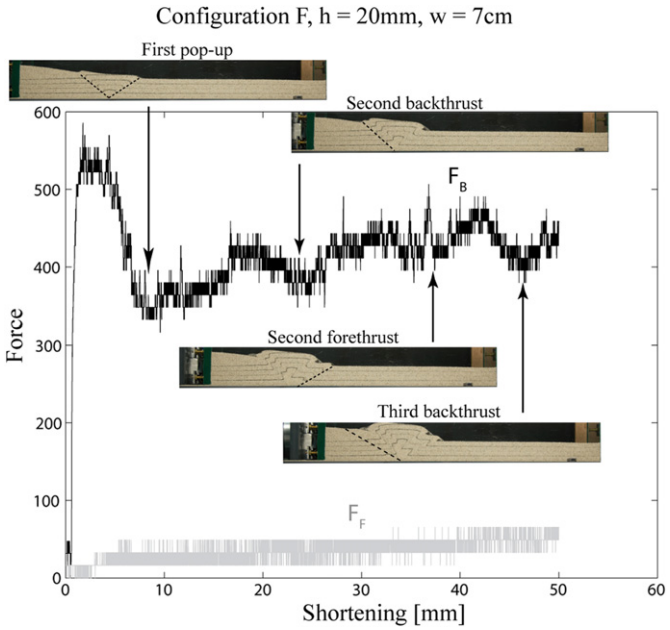

Fig. 13. Dimensionless force versus displacement in experiment 100 and associated views through a lateral wall. F_B is the force at the back wall (left wall in the photos), F_F is the force at the front wall. The mean difference between the two curves is $\bar{F}_H = 384$ (equation (4)).

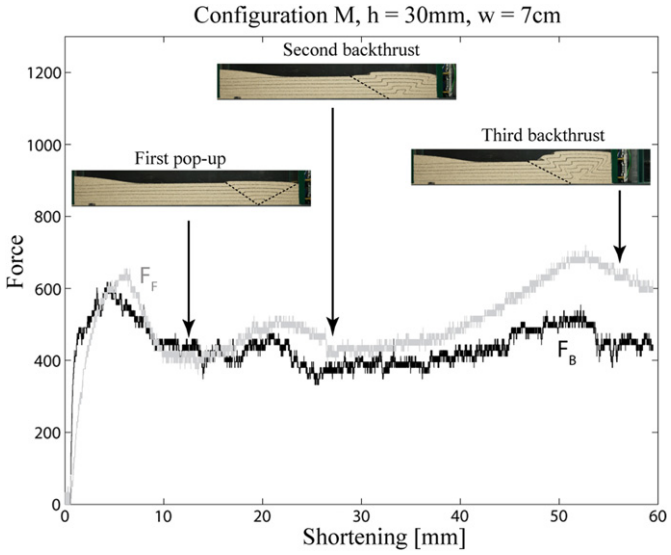

Fig. 14. Dimensionless force versus displacement in experiment 95 and associated views through a lateral wall. F_B is the force at the back wall (left wall in the photos), F_F is the force at the front wall. The mean difference between the two curves is $\bar{F}_H = -66$ (equation (4)).

narrow box diverge more importantly than the others with increasing ratio S_L/S_B. The observations of pop-up locations at $\tilde{d} = d/D > 1$ (Fig. 8) can only be explained by the dominance of frictional effects on the side walls which are not accounted for by this 2D stability theory. The best set-up is that using the wide box ($w = 28$ cm), in configuration F, because it matches best the theoretical predictions.

The question of the accuracy of this 2D solution has been addressed in Cubas (Thesis, 2009) using an inverse problem formalism that was developed for sand boxes by Maillot et al. (2007). Conclusions of this analysis are summarized in the Appendix.

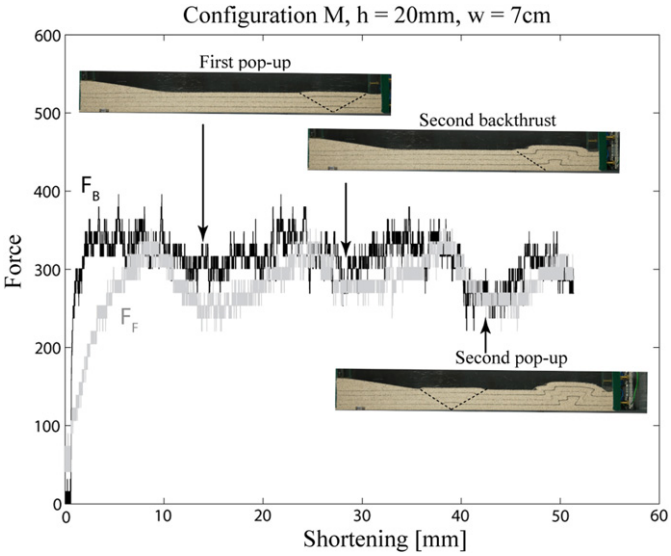

Fig. 15. Dimensionless force versus displacement in experiment 99 and associated views through a lateral wall. F_B is the force at the back wall (left wall in the photos), F_F is the force at the front wall. The mean difference between the two curves is $\bar{F}_H = 32$ (equation (4)).

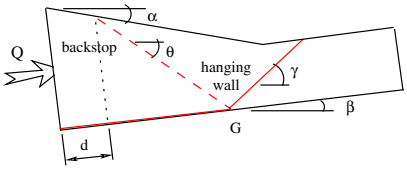

Fig. 16. Definition of the failure mode considered to determine the critical stability conditions for the wedge on a layer with the application of the maximum strength theorem.

4.4. Using different base and side wall materials

We have demonstrated bias effects due to lateral friction in the particular case where basal and lateral friction coefficients are equal. If basal friction is much lower than lateral friction, drastic biases occur, even for very small values of S_L/S_B (Vendeville, 2007). In the opposite case, the biases would be smaller (Koyi and Cotton, 2004; Costa and Vendeville, 2004). However, the difference with a 2D solution is not symmetric with respect to the experimental configuration. It appears greater in configuration M. This configuration is that of boxes using a conveyor belt. These boxes are used typically to perform experiments with very large applied shortening, at scales corresponding to whole accretionary wedges and integrating surface transport (e.g., Lohrmann et al., 2003; Konstantinovskaia and Malavieille, 2005; Hoth et al., 2007). They are usually narrow, forcing structures to be nearly plane-strain, and the evolution is thus conveniently monitored through the lateral glass walls. The ratio S_L/S_B can exceed 100%, increasing with shortening. Since the side walls are treated with great care to reduce friction with sand, and basal friction coefficients are often relatively high, it remains difficult to assess any bias introduced by side wall friction in these experiments.

Although it would be a useful result to test experimental protocols and 3D numerical simulations, an extension of the critical prism theory to account for a 3D stress field due to lateral friction is yet out of reach. At least, one should conduct experiments with large shortening in order to compare observed critical tapers with the theoretical values as done by Davis et al. (1983).

4.5. Is perfect plane-strain desirable?

It is sometimes argued that narrow boxes are useful because thrusts exhibit much less lateral variations, and would thus be less influenced by heterogeneities (due to, for example, initial imperfections of the sand body) (Schreurs et al., 2006). Following this

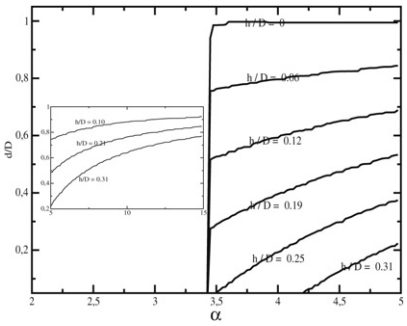

Fig. 17. The optimum distance of the backthrust to the back wall measured on the topography as a function of the wedge slope α and for different thickness h. The shock close to $\alpha = 3.9$ corresponds to Dalhen's stability transition. In inset, this optimum distance is presented for large values of α corresponding to the experimental conditions.

argument, the proper width of a sand box is a trade-off between lateral friction effects (narrow box) and lateral thrust variations (wide box). There is an alternative strategy, where lateral friction effects are reduced to the minimum (using a box as wide as possible), and lateral variations of thrusts are interpreted as intrinsic experimental variability, contributing for example to the evaluation of experimental error bars (Cubas et al., 2010). It is indeed difficult to justify an analogy of rigid lateral walls with natural structures, whereas lateral variations of thrust planes are a common natural feature.

5. Conclusion

The goal of this article is to measure the effect of the friction of sand on the lateral walls in sand box experiments. The experiments consist in the plane-strain horizontal shortening of a sand wedge with an accreting flat layer. Varying the thickness of the accreting layer and width of the box allows us to vary the surface S_L of sand in contact with the lateral walls, and the surface S_B, in contact with the basal plate of the box, from $S_L/S_B = 0.09$ to 0.92. Each experiment was repeated using two widely used configurations of the box, named here M and F, where the base is either mobile (M) or fixed (F) with respect to the lateral walls. In each configuration, lateral shear forces act in opposite directions and in different parts of the sand body. In addition, we monitored forces at the front and back walls.

The conclusions are:

$S_L/S_B < 0.1$ Thrusting is at the same location in configuration M and F throughout the box. The mean difference $\overline{F}_H$ between forces monitored at back and front walls is the same in each configuration. Therefore, lateral friction has negligible effects.
$0.1 < S_L/S_B < 0.35$, lateral friction effects are expressed by opposite thrust curvatures near the lateral walls.
$S_L/S_B > 0.35$, thrusting occurs at different locations throughout the box, thus revealing a major experimental bias. $\overline{F}_H$ is greater in configuration F than M, proving, from equilibrium conditions, that the total horizontal lateral shear force increases relative to the basal shear force when switching from F to M. In the extreme case of $S_L/S_B = 0.92$ in configuration M, the lateral shear force slightly overcomes the basal shear force, and thrusting occurs at the frontal end of the box, because of the foreward drag of the lateral walls. In addition, thrust curvatures decrease with increasing S_L/S_B ratio. Therefore, plane thrusting cannot be used as a criterion for the absence of lateral friction effect.

Based on limit analysis, we propose a generalisation of the critical prism theory to account for the presence of a flat layer prolonging the wedge. The resulting 2D predictions of the onset of thrusting for each set-up are clearly in a much better agreement with our observations in configuration F than in configuration M. These predictions are by definition free from effects of lateral walls. We conclude, as was foreseen from the force measurements, that the effect of lateral friction is much more pronounced when using configuration M.

The ratio S_L/S_B is not the only parameter controlling the relative magnitudes of the lateral and basal shear forces. If using frictional surfaces, they also depend on the normal stresses, which are not easy to measure. Also, if setting a more frictional material on the basal plate, the effect of lateral walls should be less. On the contrary, if lubricating the basal plate, one should also lubricate as much the lateral walls.

Note finally, that the two configurations M and F are physically set-up using the same pieces of glass. It is a straightforward matter to build such an experimental box. For boxes using a conveyor belt, configuration F can be set-up by attaching the lateral walls to the belt. Comparison of both configurations M and F seems to us the best way to prove the absence of bias due to the lateral walls.

Acknowledgements

We thank Florian K. Lehner for his thorough review of the manuscript. Engineer Jean-Christian Colombier from the University of Cergy-Pontoise has brought a decisive technical support.

Appendix. Stability of a sand wedge on a flat layer

The objective of this Appendix is to find the stability conditions in the sense of Dahlen (1984) for a wedge on a layer. The method relies on the maximum strength theorem, presented in Cubas et al. (2008), and consists in minimizing a family of upper bounds to the force applied at the back wall, to obtain the least upper bound.

The maximum strength theorem combines the theorem of virtual powers (weak form of equilibrium) and the fact that the stress vector acting on any velocity discontinuity has to be within the material strength domain, in the appropriate stress space (τ, σ_n plane in our problem), bounded here by the Coulomb criterion. The various upper bounds are obtained by varying three parameters of the failure mechanism presented in Fig. 16 and which consist of the two reverse faults (the fore- and the backthrust) rooting at the same point G on the décollement. The décollement is partly activated, between the back wall and point G. The two faults are velocity discontinuities between the backstop, the hanging wall and the rest of the structure at rest. The three parameters varied to minimize the upper bound are the dip of the two faults (θ and γ) and the position of point G. This upper bound reads

$$Q_u = \frac{\rho g}{\cos\phi_D}\left(S_{BS}\sin(\phi_D+\beta) + S_{HW}\sin(\gamma+\phi)\frac{\sin(\theta+\phi+\phi_D+\beta)}{\sin(\theta+\gamma+2\phi)}\right) \quad (5)$$

in which S_{BS}, S_{HW}, ρ and g are the surfaces of the backstop and of the hanging wall, the bulk material density and the gravity acceleration, respectively. The friction angles ϕ and ϕ_D are those of the bulk material and the décollement, both assumed to be cohesionless. The minimization of these upper bounds to obtain the least is done numerically following the algorithm given in the Appendix of Cubas et al. (2008) which essentially relies on a discretization of the topography and the décollement.

The relevance of this least upper bound to predict the onset of thrusting in analogue experiments has been justified by Cubas (thesis, 2009). A series of analogue experiments corresponding to the prototype in Fig. 16 was conducted with a sufficiently wide sand box to avoid the side effects of interest in this contribution. The least upper bound obtained from equation (5) was used in an inverse analysis to predict the first failure mode. The observables included the three parameters minimized here and the least error between theory and measure provided the probability distribution of the material parameters, including the friction angles used here. It was shown that the independent measures of these two material properties were consistent with the results of the inverse method, justifying the proposition to use our theory to predict the outcome of analogue experiments with sand.

The application of equation (5) proposed here is to find the stability transition from sub-critical to super-critical as the topography angle α is increased. The critical stability conditions for which failure occur anywhere by faulting within the triangular wedge correspond in our theory to the indeterminacy of the position of point G: the root of the two faults could be anywhere on the

décollement and thus faulting is also occurring within the wedge at any position. The extension of these conditions to the wegde on a layer is discussed next.

Results obtained for the geometrical properties of the sand box build in the laboratory are presented in Fig. 17. The friction angle for the sand and the décollement are set to 30° and 10°, respectively. The optimum distance d, defined in Fig. 1 and associated to the three parameters which minimizes equation (5), is presented as a function of the wedge topographic dip α for various values of the thickness h normalized by the wedge length D.

The optimum d for small values of α is zero. The backthrust is thus outcropping at the contact of the back wall. For the critical value of $\alpha_c = 3.4°$, the optimum distance d increases sharply to reach a value close to one. This critical α_c is the one predicted by Dahlen (1986). For $\alpha < \alpha_c$ the wedge is sub-critical and the failure mode is at the back, the closest possible to the back wall. For $\alpha > \alpha_c$, the wedge is super-critical and the failure mode is at the front of the wedge and requires the activation of the main part of the décollement.

The maximum strength theorem captures exactly Dahlen's transition for the wedge with no layer ($h/D = 0$). Dahlen's solution is not applicable to non-zero h whereas the maximum strength theorem remains applicable. For values of h/D less than 0.19, the sharp stability transition is still present at the same α_c. The distance d is an increasing function of α for super-critical wedges. Note that the shock in d at α_c is decreasing with increasing h. For larger values of h/D, greater than 0.25, one notices that there is no shock. There is even a delay in α_c before the distance d starts to increase with α. This difference between small and large values of h is due to the geometry of the failure mechanism. For small values of h, the failure mechanisms and in particular the forethrust outcrops on the topographic slope of the wedge. For larger h, the same thrust is within the layer even for $d =$ zero obtained for sub-critical wedges. The two structures have thus different failure mechanisms. Note that for the larger h, d keeps on increasing with α for super-critical conditions even for rather large values of α, relevant to the experiments presented here (see inset of Fig. 17).

The first conclusion is that Dahlen's stability condition is still applicable to a wedge on a layer as long as its thickness is less than $D/4$, approximately. For larger h, the structure should not be interpreted as a wedge since the failure mechanisms affects both the layer and the wedge. The second conclusion is that the 2D stability condition for α close to 10° is super-critical for any h.

References

Bjerrum, L., Kringstad, S., Kummeneje, O., 1961. The shear strength of a fine sand. In: Proceedings of 5th International Conference Soil Mechanics and Foundation Engineering, vol. 1, pp. 29–37.

Buiter, S.J.H., Babeyko, A.Y., Ellis, S., Gerya, T.V., Kaus, B.J.P., Kellner, A., Schreurs, G., Yamada, Y., 2006. The numerical sandbox: comparison of model results for a shortening and an extension experiment. In: Buiter, S.J.H., Schreurs, G. (Eds.), Analogue and Numerical Modelling of Crustal-scale Processes. London Geol. Soc. Spec. Publ., pp. 29–64.

Costa, E., Vendeville, B., 2004. Experimental insights on the geometry and kinematics of fold-and-thrust belts above weak, viscous evaporitic décollement: reply to comments by Hemin Koyi and James Cotton. J. Struct. Geol. 26, 2139–2143.

Cubas, N., Leroy, Y.M., Maillot, B., 2008. Prediction of thrusting sequences in accretionary wedges. J. Geophys. Res. 113, B12412. doi:10.1029/2008JB005717.

Cubas, N., 2009. Séquences de chevauchements, Prédictions mécaniques, validation analogique et application à la chaîne de l'Agrio (Argentine). Thèse de doctorat de l'Université de Paris-sud.

Cubas, N., Maillot, B., Barnes, C., 2010. Statistical analysis of an experimental compressional sand wedge. J. Struct. Geol. 32 (6), 818–831.

Davis, D., Suppe, J., Dahlen, F.A., 1983. Mechanics of fold-and-thrust belts and accretionary wedges. J. Geophys. Res. 88 (B2), 1,153–1,172.

Dahlen, F.A., 1984. Noncohesive critical Coulomb wedges: an exact solution. J. Geophys. Res. 89 (B12), 10,125–10,133.

Egholm, D.L., Sandiford, M., Clausen, O.R., Nielsen, S.B., 2007. A new strategy for discrete element numerical models: 2. Sandbox applications. J. Geophys. Res. 112, B05204. doi:10.1029/2006JB004558.

Hoth, S., Hoffmann-Rothe, A., Kukowski, N., 2007. Frontal accretion: an internal clock for bivergent wedge deformation and surface uplift. J. Geophys. Res. 112, B06408. doi:10.1029/2006JB004357.

Klinkmüller, M., Rosenau M., Boutelier, D., Kemnitz, H., Schreurs, G., 2008. Properties benchmark of granular and viscous analogue materials. Bollettino di Geofisica, vol. 49, extended abstract, Geomod2008, Firenze.

Konstantinovskaia, E., Malavieille, J., 2005. Erosion and exhumation in accretionary orogens: experimental and geological approaches. Geochem. Geophys. Geosyst. 6 (2). doi:10.1029/2004GC000794.

Koyi, H.A., Cotton, J., 2004. Experimental insights on the geometry and kinematics of fold-and-thrust belts above weak, viscous evaporitic décollement; a discussion. J. Struct. Geol. 26, 2139–2143.

Krantz, R.W., 1991. Measurements of friction coefficients and cohesion for faulting and fault reactivation in laboratory models using sand and sand mixtures. Tectonophysics 188, 203–207.

Lohrmann, J., Kukowski, N., Adam, J., Oncken, O., 2003. The impact of analogue material properties on the geometry, kinematics, and dynamics of convergents and wedges. Journal of Structural Geology 25, 1691–1711.

Maillot, B., Barnes, C., Mengus, J.-M., Daniel, J.-M., 2007. Constraints on friction coefficients by an inverse analysis of sand box thrust dips. J. Struct. Geol. 29, 117–128.

Marshak, S., Wilkerson, M.S., 1992. Effects of overburden thickness on thrust belt geometry development. Tectonics 11, 560–566.

Marques, F.O., Cobbold, P.R., 2006. Effects of topography on the curvature of fold-and-thrust belts during shortening of a 2-layer model of continental lithosphere. Tectonophysics 415, 65–80.

Nieuwland, D.A., Urai, J.L., Knoop, M., 2000. In-situ stress measurements in model experiments of tectonic faulting. In: Aspects of Tectonic Faulting: In Honour of Georg Mandl. Springer.

Schreurs, G., Buiter, S.J.H., Boutelier, D., Corti, G., Costa, E., Cruden, A.R., Daniel, J.-M., Hoth, S., Koyi, H.A., Kukowski, N., Lohrmann, J., Ravaglia, A., Schlische, R.W., Oliver Withjack, M., Yamada, Y., Cavozzi, C., Delventisette, C., Elder Brady, J.A., Hoffmann-Rothe, A., Mengus, J.M., Montanari, D., Nilforoushan, F., 2006. Analogue benchmarks of shortening and extension experiments. In: Buiter, S.J.H., Schreurs, G. (Eds.), Analogue and Numerical Modelling of Crustal-scale Processes. Geological Society, London, Special Publication 253, pp. 1–27.

Vendeville, B.C., 2007. The 3-D Nature of Stress Fields in Physical Experiments and Its Impact on Models Overall Evolution. Sollicited Oral Contribution. 15–20 April, 2007. EGU General Assembly, Vienna.

Wibberley, C.A.J., 1997. Three-dimensional geometry, strain rates and basement deformation mechanisms of thrust-bend folding. J. Struct. Geol. 19, 535–550.

Wygal, R.J., 1963. Construction of models that simulate oil reservoirs. Soc. Pet. Engineers J., 281–286.